# PCCP

## PAPER

# *In situ* non-aqueous nucleation and growth of next generation rare-earth-free permanent magnets†

Hyojung Yoon,[ab] Aoran Xu,[a] George E. Sterbinsky,[c] Dario A. Arena,[c] Ziying Wang,[a] Peter W. Stephens,[d] Ying Shirley Meng*[ab] and Kyler J. Carroll*[ae]

Using a controllable wet chemical approach, the polyol process, we developed a cobalt carbide nanomagnet consisting of an assembly of $Co_2C$ and $Co_3C$ nanoparticles as an alternative to rare earth permanent magnets (PMs). The thermodynamically stable mixed phase cobalt carbide nanoparticles are shown to be acicular in morphology. Their exchange-coupled magnetic interaction possessing high maximum energy product of 20.7 kJ m$^{-3}$ and room temperature coercivity (2.9 kOe) has been confirmed through vibrating sample magnetometer (VSM) and first order reversal curves (FORCs). These metastable carbide nanoparticles offer improved magnetic properties compared to their pure bulk form. An understanding of the formation mechanism, using *in situ* time-resolved X-ray spectroscopy (TR-XAS), and the correlation between phase contributions to the properties are described in detail. Our strategy presents a controllable route to preparing the cobalt carbide nanomagnets, which could be potentially useful in permanent magnet clean energy applications. Additionally, the *in situ* apparatus offers a promising way to directly explore the effects of reaction variables for high-temperature wet chemical reactions.

## Introduction

A ferromagnetic material based upon nanoscale cobalt carbide had been recently shown to exhibit unusually large coercivities and energy products, $(BH)_{max}$.[1,2] This nanoscale cobalt carbide is especially attractive since it provides a rare-earth-free alternative to currently existing high performance permanent magnets. The particular properties realized by this material are highly dependent upon the processing conditions, where coercivity is shown to vary inversely with saturation magnetization. Therefore, developing a fundamental understanding of the effect of those conditions on the material's magnetic properties is critical to translate it into a realistic candidate, which can compete with rare-earth based magnets. Elucidation and control over nucleation and growth at the nanoscale has been of notable interest over the past decade since many chemical and physical properties can be vastly different than their bulk counterparts.[3,4] This is particularly

true in the case of cobalt carbide, which has an anomalously high magnetic energy density at the nanoscale.

In recent years, there has been extensive research into the fabrication of nanocrystalline metals with uniform size and shape by utilizing several processing techniques such as: thermal decomposition, photochemical reduction, pulsed laser ablation, as well as several chemical synthesis methods.[5–7] In particular, the chemical synthesis methods offer a more efficient route to obtaining nanocrystalline material of tunable size and shape. The polyol process, in which metal salts are reduced by a polyalcohol, has provided a simple and versatile approach to producing well-defined nanoscale materials by effectively separating the nucleation and growth steps.[8–10] Nevertheless, despite many reports elucidating mechanisms for the growth of nanoparticles with enhanced properties, wet chemical synthesis methods remain an art rather than a science. As such, many methods to manufacture nanocrystalline materials have failed to reach the industrial level. A major complication is the variation of the kinetics depending on the synthetic parameters such as pH, metal precursor concentration, temperature, capping agents, and reaction time. To get a precise synthetic system at the level needed for large-scale production, a more detailed study of the nucleation and growth kinetics is needed. *In situ* TR-XAS has been recently proven to be a powerful method to monitor the dynamic structural changes and kinetics during the formation of nanocrystalline materials. As *in situ* techniques are becoming more commonplace in research, reports on the direct monitoring of the nucleation and growth of nanocrystalline

[a] *Department of NanoEngineering, University of California San Diego, La Jolla, CA 92093, USA. E-mail: shmeng@ucsd.edu*

[b] *Materials Science and Engineering program, University of California San Diego, La Jolla, CA 92093, USA*

[c] *National Synchrotron Light Source, Brookhaven National Laboratory, Upton, NY 11973, USA*

[d] *Department of Physics and Astronomy, Stony Brook University, Stony Brook, NY 11794, USA*

[e] *Chemical Engineering, Massachusetts Institute of Technology, Cambridge, MA 01239, USA. E-mail: kcarroll@mit.edu*

† Electronic supplementary information (ESI) available. See DOI: 10.1039/c4cp04451g

metals at room temperature using *in situ* TR-XAS are being developed.[11] Many reports describe room temperature photoreduction of catalytically active materials such as gold colloids, platinum, rhodium, and palladium.[12–16] Despite these recent attempts to monitor the nucleation and growth of nanocrystalline materials, there still lacks direct observation of high-temperature solution based syntheses. This is of particular importance, as most systems used to synthesize nanocrystalline materials require high operating temperatures in addition to complex reaction chemistries.

Here we report the kinetics of nucleation and growth for cobalt metal and carbide nanocrystals formed using a polyol process, with reaction temperatures >300 °C, using a custom designed reactor. The nanoparticles offer unusual magnetic properties, a high maximum energy product and coercivity, and these properties change with particle size, morphology and ratio of mixing particles. In order to effectively control these variables and thereby optimize the magnetic properties of the system, a detailed understanding of the effects of changes in synthesis parameters is essential. The important role of surfactants and reaction duration on the phase formation and magnetic properties has been illuminated. In this work, through *in situ* TR-XAS, we show that the nucleation and growth of metastable cobalt carbide *via* the polyol process proceeds through thermodynamically stable cobalt nuclei up to a critical size; below this critical size, carbide formation is kinetically favored while above that size, metal is the more likely outcome. We also demonstrate how the concentration dependences follow general nucleation and growth theories.

## Experimental

### Synthesis of cobalt carbide nanoparticles

All Chemicals were used without any further purification. In a typical procedure, 0.1 M cobalt chloride ($CoCl_2 \cdot 6H_2O$, guaranteed reagent, Spectrum Chemical) as a cobalt precursor is dissolved in 100 ml of tetraethylene glycol (TTEG; $C_6H_{18}O_5$, Spectrum Chemical), followed by the addition of potassium hydroxide (KOH, ≥85%, ACS reagent, Sigma-Aldrich). In a typical cobalt carbide reaction, a cobalt precursor salt ($CoCl_2 \cdot 6H_2O$) and KOH are dissolved in TTEG within the designed *in situ* reactor equipped with stirrer and a reflux condenser and heated to 300 °C. The reaction was allowed to proceed for up to 2 h.

### Material characterization

Powder X-ray diffraction (XRD) patterns of the cobalt metal and carbide nanoparticles were obtained at the X16C high-resolution powder diffraction station at the National Synchrotron Light Source. Retrieved samples for powder XRD were sealed in Lindemann glass capillaries. X-rays of approximately 0.7 Å wavelength were selected by a channel-cut Si(111) monochromator, calibrated for each run with NIST standard reference material 1976 ceramic corundum plate. The sample was spun during data collection to insure good particle counting statistics. Diffracted X-rays were analyzed by a single Ge(111) crystal before a commercial scintillation counter. Measured intensity was normalized to incident flux, measured by an ion chamber in the incident beam path open to the atmosphere.

Data were collected in step-scan mode, with collection time typically linearly proportional to diffraction angle $2\theta$. Rietveld refinements of crystalline phases of $Co_2C$ and $Co_3C$ were performed with TOPAS-Academic software. The non-crystalline structure of the Co sample was modeled with DIFFaX. More details are given in the ESI.† Morphological features were examined by a transmission electron microscope (TEM) and a field-emission scanning electron microscope (FESEM). SEM images were collected using a Phillips XL30 ESEM at an accelerating voltage of 20 kV. High-resolution TEM images and selected area electron diffraction (SAED) patterns were taken on a JEOL 3000F transmission electron microscope operated at 300 kV. The samples for TEM studies were prepared by drying a drop of the aqueous suspension of nanoparticles on a carbon-coated copper grid (Ted Pella, Redding, CA).

### Magnetic properties

Magnetic properties were measured using a Quantum Design-Versalab vibrating sample magnetometer (VSM). The Hysteresis loop was carried out using a maximum magnetic field of 3 kOe, with a field sweep rate of 100 Oe s$^{-1}$. Isothermal remanence magnetization (IRM) plots were collected from 0 to 10 kOe with step of 100 Oe. The direct current demagnetization (DCD) plots were collected in the same manner as the IRM plots, except that the particles were first saturated in a field of −30 kOe. A Henkel plot was then created by $\delta M = (M_{DCD} - M_R + 2 \times M_{IRM})/M_R$. A set of FORCs was obtained by: (1) saturating the sample by applying a field $H_{max}$ = 20 kOe, (2) reducing the field to a return value $H_r$, where $H_r < H_{max}$, (3) increasing $H$ to $H_{max}$ again and measuring the magnetization $M(H,H_r)$, (4) repeating steps (2) and (3) for decreasing value of $H_r$ where $H_r > -H_{max}$.

### *In situ* TR-XAS analysis

For the time-resolved *in situ* analysis, we developed *in situ* TR-XAS reactor (Fig. 1). The reactor was made with aluminum (Al) in order to withstand the high operating temperatures along with the high alkaline synthetic conditions required for reaction; the Al reactor also distributes the heat evenly, thereby minimizing local temperature variations. An X-ray transparent, high-temperature, polyimide film was integrated into the reactor as a window for *in situ* TR-XAS. Temperatures were provided by implanted cartridge heaters and a copper cooling system with a k-type thermocouple providing feedback to a control box. The *in situ* study involves analyzing the X-ray absorption near edge structure (XANES) and the extended X-ray absorption fine structure (EXAFS) of the Co K-edge (7709 eV). We monitor the fluorescent X-ray intensity ($I_f$) using a Passivated Implanted Planar Silicon (PIPS) detector, where $\mu(E) = I_f/I_0$. Time-resolved X-ray analysis was obtained by collecting a full spectrum (XANES and EXAFS) in 100 ms using a rotating Si monochromator at X-18B at NSLS.

## Results and discussion

### Polyol synthesis of cobalt metal and carbide

A major attraction of the polyol process is the ability to vary the polyalcohol chain length, which in-turn enables control over
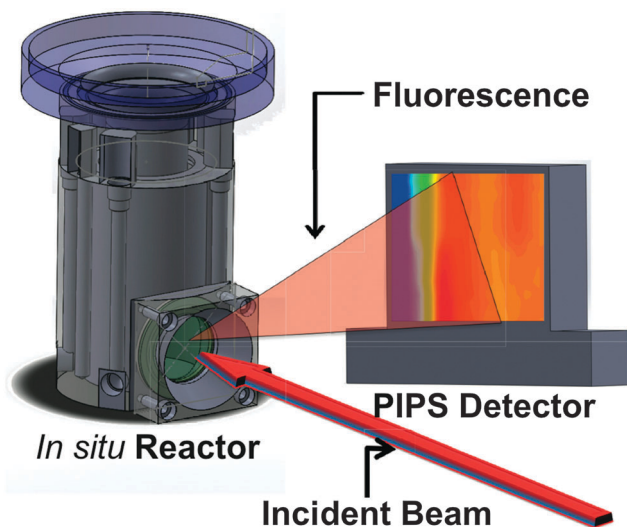
This journal is © the Owner Societies 2015

*Phys. Chem. Chem. Phys.*, 2015, **17**, 1070–1076 | **1071**

Fig. 1 General schematic of a designed *in situ* cell for measurement of time-resolved XAS.



Fig. 2 High-resolution powder X-ray diffraction patterns for Co metal (a) and carbide (b).

the operating temperatures. For example, the operating temperature of ethylene glycol is about 197 °C while TTEG is about 314 °C.

The operating temperature is merely a few degrees below the boiling point (bp) of the solvent, where the polyalcohol is the most reactive.[4,17,18] The synthesis of cobalt carbide has been shown to require high operating temperatures, 300 °C, and thus TTEG was the polyol solvent of choice (bp = 325 °C).[1,2] From our previous study,[2] we have already shown that the delicate control of the specific carbide phase can be obtained through the addition of various amounts of KOH in the solution. The hydroxide concentration has been shown to induce polymerization and the formation of polyethylene glycol (PEG). Increasing the hydroxide concentration results in longer PEG chains which causes variations in the nucleation dynamics. To probe the nucleation and growth kinetics and their dependence on precursor metal salt and hydroxide concentration, two separate reaction conditions were investigated. Detailed conditions are described in Table S1 (ESI†). Varying synthetic parameters resulted in either the formation of the thermodynamically stable $Co^0$ metal phase or the metastable carbide phase. The structural properties of resulted nanoparticles were investigated using *ex situ* synchrotron XRD. In Fig. 2a, the powder XRD pattern of Co metal could not be fit as one or more crystalline phases. Bulk Co has a hexagonal close packed (HCP) equilibrium structure at ambient conditions and has a martensitic transition to face centered cubic (FCC) at high temperatures; the subtle energy difference between the two phases leads to a variety of metastable and intergrowth forms.[19,20] DIFFaX[21] was used to model such structures, with parameters adjusted to produce qualitative agreement with the data shown in Fig. 2a. In this model, the characteristic dimensions of domains of each type were ~8 atomic layers, and the triangular close-packed layers had a lateral extent on the order of 75 atoms. The nearest neighbor distance within and between layers was 2.50(1) Å. Note the stronger, sharper peaks where FCC and HCP peaks coincide, and the clear broadening and suppression of the
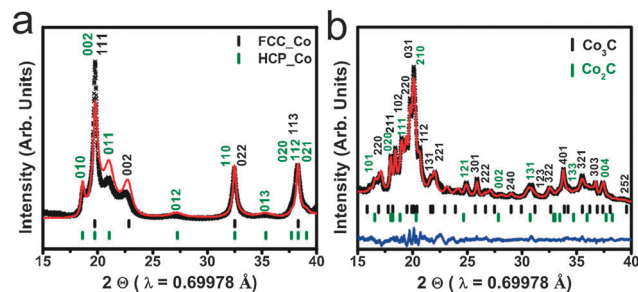
HCP (012) and (013) peaks at $2\theta$ = 27.2° and 35.3°, respectively. The fit is not sufficiently good to be regarded as a structural model for the phase, but it is a useful first approximation. All the reflections shown in Fig. 2b can be indexed in the orthorhombic system using the *Pnnm* and *Pnma* space group. Rietveld refinements of crystalline phases of $Co_2C$ and $Co_3C$ were performed with TOPAS-Academic software.[22] The results of the Rietveld crystallographic analysis and crystal structures of the cobalt carbide samples are given in the Table S2 and Fig. S1 (ESI†).

Fig. 3a and b depict SEM images of the resultants at two different synthetic conditions. SEM observations show agglomerated particle clusters, consisting acicular or rod-like morphology. An interesting feature of cobalt carbides was that they tended to stack vertically on their edges; therefore, they formed flower-like architectures. To obtain structural information, we conducted high-resolution TEM, shown in Fig. 3c and d. A thin layer of carbon is consistently observed at the edge of the cobalt metal particles (Fig. 3c). A similar observation was found through the micro-Raman measurement (see Raman spectra in Fig. S3, ESI†). The HRTEM image in Fig. 3c, which was taken near the [001] zone axis, with a 0.22 nm *d*-spacing value, corresponds to the cobalt metal on the (100) plane. The [010] direction was found to
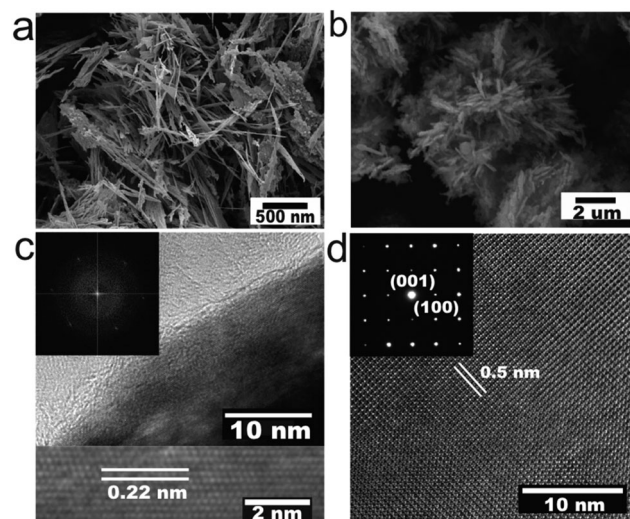


Fig. 3 SEM images of Co metal (a) and carbide (b), high-resolution TEM images and insets of SAED patterns for representative Co metal (a, c) and carbide (d).

1072 | *Phys. Chem. Chem. Phys.*, 2015, **17**, 1070–1076

This journal is © the Owner Societies 2015

typically lie along the long axis of the $Co_3C$ crystallites in Fig. 3d. The lattice spacing was also determined to be about 5.0 Å along that direction. Aggregated nanometer-scaled crystals were observed with magnetic domain boundaries through Lorentz microscopy (in Fig. S4, ESI†). The inset in Fig. 3d shows a typical SAED pattern recorded by directing the electron beam perpendicular to the flat faces of an individual particle. The SAED pattern shows the corresponding diffraction pattern, indexed to the [010] direction of $Co_3C$.

## Magnetic properties of cobalt metal and carbide

The magnetic behaviors of synthesized cobalt carbide nanoparticles were investigated and compared with synthesized cobalt metal. While the cobalt metal shows a high saturation magnetization with a low coercivity, the carbide sample has a high coercivity ($\sim$2.9 kOe). That leads a 70% increase in the energy product ($BH_{max}^{Co-carbids} \approx$ 15.84 MGOe) as shown in Fig. 4. Henkel plots (in Fig. 5a and b), which can be obtained from isothermal remanent magnetization (IRM) and direct current demagnetization (DCD) tests, were carried out to better investigate the interaction mechanism and associated strength in these two systems based on Stoner–Wohlfarth theory: $\delta M = (M_{DCD} - M_R + 2 \times M_{IRM})/M_R$,[23,24] where $M_R$ represents the remanent magnetization. Both the cobalt metal and carbide show a positive $\delta M$ value, which refers to a dominant short-range exchange interaction. The highest intensity peak appears around the coercivity field, where the angle $\phi$ between two single magnetic particles becomes largest.[25] In Fig. 5c and d, first order reversal curves (FORCs) provide information pertaining to the switching field distribution and give insight into interaction mechanisms between particles in the system.[26,27] FORC contours are generated by calculating the second derivative, $\rho(H, H_r) \equiv -\frac{1}{2}\frac{\partial^2 M(H, H_r)}{\partial H_r \partial H}$. The local coercivity field ($H_c$) and bias interaction field ($H_u$) are
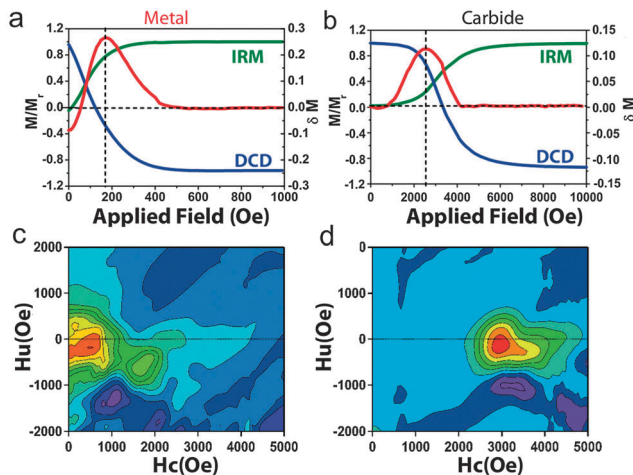


Fig. 5 (a) and (b) The isothermal remanence (IRM), DC demagnetization (DCD) remanence curves, and Henkel plots for Co metal and carbide. (c) and (d) First-order reversal curve (FORC) diagrams for Co metal and carbide.

obtained by a coordinate transformation: $H_c = (H - H_r)/2$. and $H_u = (H + H_r)/2$, where the $H_r$ is the coercivity of the remanence. For assemblages of randomly orientated, non-interacting, single domain (SD) grains, the FORC diagram displays an asymmetric "boomerang" shape contour line with the central intensity peak.[27] The negative deviations of $\rho$ on the $H_u$ axis reveal that exchange interaction is dominant in both cobalt metal and carbide systems, which are in accordance with the Henkel plot results. The non-uniform and spread tails of the switching field distribution on the $H_c$ axis in cobalt metal provides evidence of asynchronous reversal behavior caused by polydisperse grain sizes and anisotropy within the system.[28] However, the cobalt carbide system has a single-phase magnetization reversal, at 3 kOe, indicating an exchange-coupled system with a narrow size distribution.

## Nucleation and growth probed by *in situ* TR-XAS measurement

To reveal how the synthetic conditions affect nanoparticle synthesis, the dynamics of the cobalt metal and carbide formation were investigated as a function of reaction time. In order to analyze the formation kinetics by using the appropriate rate equation, we proposed the overall reaction mechanism as shown in Scheme 1, where the metal nanoparticle formation is a two-step process.[4] The initial reaction rate, $k_1$, designates the ligand exchange forming the cobalt–glycolate species, which occurs once the metal salt precursor is dissolved in the polyol. The reaction rate, $k_2$, covers the progressive conversion of cobalt–glycolate to $Co^0$ utilizing the electrons from the carbon center to form a double bond with the oxygen atom.[4] The time evolution for Co K-edge *in situ* TR-XAS spectra during polyol process for total reduction time of 100 min are plotted in Fig. 6a and b using a color scale for the spectrum intensity. To clearly show the reduction of $Co^{2+}$ to $Co^0$, selective XANES and EXAFS spectra are presented in Fig. 6c and d. As presented in the XANES spectra, the magnitude of $Co^{2+}$ absorption around 7718 eV largely disappeared after intermediate state and shifted towards lower energy in both reactions, corresponding to metallic $Co^0$ by
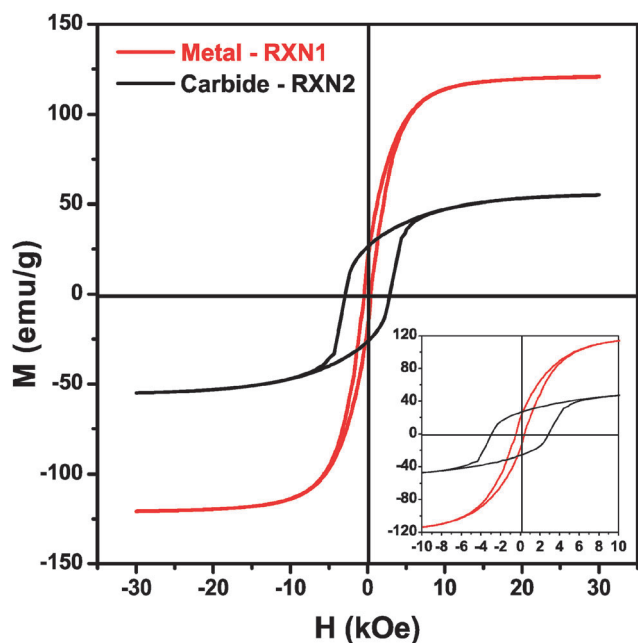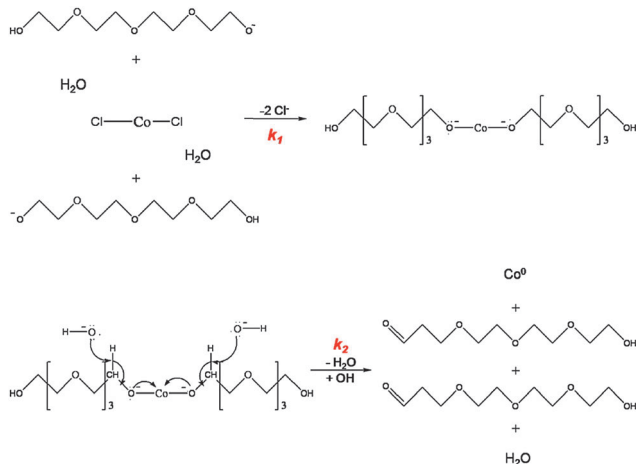


Fig. 4 Hysteresis loops obtained from a VSM measured operating at room temperature for Co metal and carbide nanoparticles.

This journal is © the Owner Societies 2015

*Phys. Chem. Chem. Phys.*, 2015, **17**, 1070–1076 | **1073**

**Scheme 1** Proposed mechanism for the formation of Co nanoparticles synthesized from TTEG solution of $CoCl_2$ in the presence of KOH.

the polyol process. It can be also confirmed through the EXAFS spectra of the *in situ* reactions that the absence of the Co–Cl contribution and the presence of the Co–Co contribution for the final phase are consistent with the reduction of $Co^{2+}$ to $Co^0$. By checking the white line intensity $\mu(E_{CoCl_2} = 7718 \text{ eV})$ and intrinsic peak—$E_{Co-Metal} = 7757$ and $E_{Co-Carbide} = 7784$ eV attributed primarily to Co–Co and Co–C bond respectively (see Fig. S5 and S6, ESI†)—quantitative kinetic values were analyzed from the *in situ* TR-XAS spectra. Concentration data as well as the fitting curves derived from reaction models are shown in Fig. 7. Details of the determination of concentration data are provided in part 4 of the ESI.† The induction period is observed for the first 1250 and 500 s in Fig. 7a and b, respectively. This duration corresponds to the accumulation of the critical concentration of Co atoms necessary

for the nucleation to occur in the original LaMer model.[29] Distinctly, in Fig. 7b, the rapid onset of the nucleation (∼500 s) resulted in a smaller induction period over the cobalt metal formation. The formation of cobalt metal and carbide phases shows a strong dependence on the induction time within the nucleation stage. To obtain detailed rate constants from the raw data curve fitting, the Avrami–Erofe'ev (AE)[30,31] and Finke–Watzky (FW)[32] models were applied. The kinetic studies of the solution based nucleation and growth of crystals are often described by the AE model, expressed as mole fraction term:

$$\alpha = 1 - \exp[-(kt)^n]$$

On the other hand, the FW 2-step model[32] is able to provide quantitative rate constants corresponding to the nucleation and growth process respectively. The FW 2-step model can be described without explicit concentration-dependence terms;[12]

$$\alpha = 1 - \frac{k_1 + k_2'}{k_2' + k_1 \exp[(k_1 + k_2')t]}$$

With these models, we determined the reaction rates *via* least squares fitting of the concentration data derived from *in situ* TR-XAS (Table S3, ESI†). It is found that the induction period is drastically shortened with a decrease of $[Co^{2+}]/[OH^-]$. Our fitting results clearly show a difference in nucleation rate, $k_1$. Comparing $k_1$ of the cobalt metal and carbide formation, $k_1^{carbide}$ is much larger than $k_1^{metal}$. It has been shown that hydroxyl ions provide nucleation sites for the formation of metallic particles.[33] This fact demonstrates that more seeds will be formed since there are enough nucleation sites, leading to the very rapid nucleation rate at high concentration of hydroxyl ions, which results in much smaller particle size. A critical size of $Co^0$ nuclei is essential to forming the desired carbide phase, as we believe that the formation of cobalt carbide is
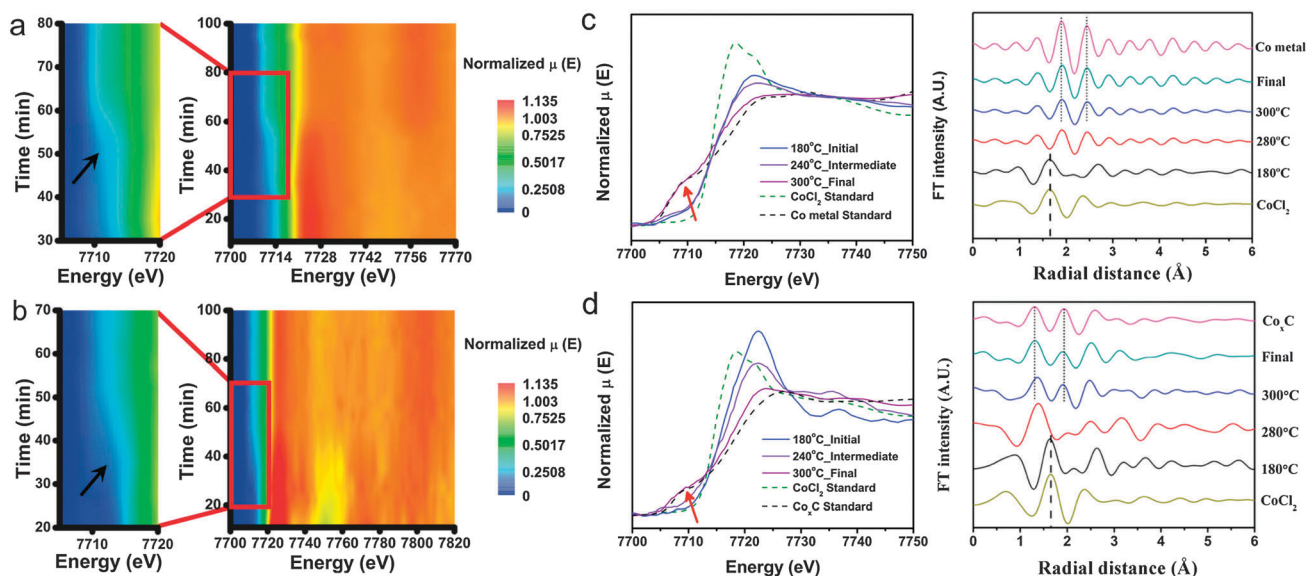


**Fig. 6** (a) Time evolution as a function of the reduction time for Co K-edge XANES spectra and color scale for the spectra intensity for Co metal formation. (b) Time evolution as a function of the reduction time for Co K-edge XANES spectra and color scale for the spectra intensity for Co carbide formation. XANES and EXAFS spectra at Co K-edge of initial, intermediate and final state during *in situ* Co metal (c) and Co carbide (d) reactions including $CoCl_2$, $Co_xC$ and Co metal powder standards.
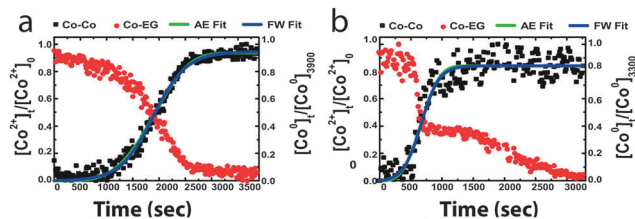
**1074** | *Phys. Chem. Chem. Phys.,* 2015, **17**, 1070–1076

This journal is © the Owner Societies 2015

**Fig. 7** Plots of $[Co^{2+}_{precursor}]_t/[Co^{2+}_{precursor}]_0$ and (a) $[Co^0_{metal}]_t/[Co^0_{metal}]_{3900}$, and (b) $[Co^0_{carbide}]_t/[Co^0_{carbide}]_{3300}$ as a function of the reduction time on the basis of the temporal change of normalized $\mu$. Curve fitting to the experimental data was carried out on the basis of the AE or FW model for the kinetics.
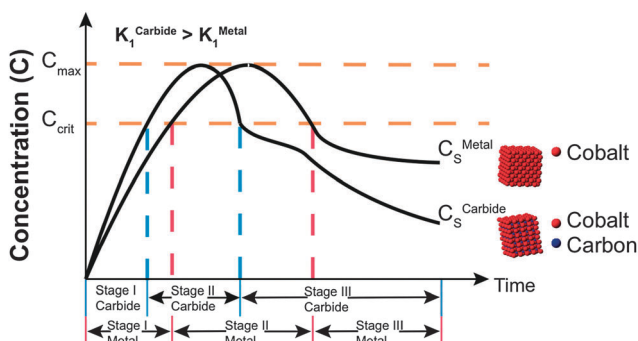


**Fig. 8** The proposed pathways for Co metal and carbide formation, as described by kinetic models obtained from the *in situ* TR-XAS data.

due to a surface reconstruction/diffusion of C atoms into the Co structure by Fischer–Tropsch reaction with the source of carbon monoxide being the aldehyde formed during the reduction of cobalt.[34–37] In Fig. 8, the graph depicts the hypothesized pathways as described in the nucleation and growth kinetic model based on the fitted parameters. The plateau region, observed in Fig. 7b, supports our previous assessment that once the critical nanosized Co nuclei are formed, they immediately act as a catalyst, whereby the carbon monoxide is catalytically decomposed to C atoms. This reaction permits carbon diffusion into the Co interstitial sites through a surface diffusion mechanism and hence results in formation of cobalt carbide.[1,2] Therefore, the cobalt nuclei should have a critical maximum size, which can be achieved with a fast enough nucleation rate to enable them to fully incorporate carbon into their structure. Recently, it is reported[38] that when two final phases, Co metal and carbide in our case, compete from the same dissolved precursor at the beginning of the reaction, the phase, with the lower energy barrier, prefers to form more rapidly as the rate of nucleation is proportional to $e^{-\Delta G/k_B T}$, where $\Delta G$ is the Gibbs free energy of a particle growing from solution,[39] $k_B$ is the Boltzmann constant and $T$ is temperature. We believe that the fast rate of nucleation helps to form cobalt carbide phase, which has a lower energy barrier of the formation than metal.

## Conclusions

We have demonstrated the polyol synthesis of mixed phase cobalt carbide ($Co_2C$ and $Co_3C$) nanoparticles having high maximum energy product (15.48 MGOe). During the polyol synthesis, the effects of reaction parameters on the magnetic properties and composition of resultants were examined. By changing the $[Co^{2+}]/[OH^-]$ concentration ratio, while keeping cobalt content constant, the resultant particles exhibited different structural and magnetic properties due to their nucleation and growth rate variation. When the $[Co^{2+}]/[OH^-]$ concentration ratio was 0.17, cobalt carbide nanoparticles showed strong exchange-coupled system with narrow size distribution. Otherwise, it gave cobalt metallic particles. The *in situ* TR-XAS measurements and analysis has been clearly shown that hydroxyl ions concentration within the solution affects nucleation rate for formation of cobalt carbide nanoparticles. The methods applied in this study can be used to tune synthesis parameters in order to achieve strongly exchange-coupled nanoparticles in similar systems. In particular, the *in situ* methods, and the insights they provide on the synthesis kinetics, permit materials scientists to significantly narrow down the very large parameter space that exists in optimizing synthesis protocols for the purpose of making large batches of magnetic nanoparticles. Thus, the result reported in this study is an important step in attenuating the critical-materials aspects of rare-earth elements and satisfying the ever-increasing demand for permanent magnets for clean technology applications.

## Notes and references

1 V. G. Harris, Y. Chen, A. Yang, S. Yoon, Z. Chen, A. L. Geiler, J. Gao, C. N. Chinnasamy, L. H. Lewis, C. Vittoria, E. E. Carpenter, K. J. Carroll, R. Goswami, M. A. Willard, L. Kurihara, M. Gjoka and O. Kalogirou, *J. Phys. D: Appl. Phys.*, 2010, **43**, 165003.

2 K. J. Carroll, Z. J. Huba, S. R. Spurgeon, M. C. Qian, S. N. Khanna, D. M. Hudgins, M. L. Taheri and E. E. Carpenter, *Appl. Phys. Lett.*, 2012, **101**, 012409.

3 C. L. Kuo and K. C. Hwang, *Chem. Mater.*, 2013, **25**, 365–371.

4 K. J. Carroll, J. U. Reveles, M. D. Shultz, S. N. Khanna and E. E. Carpenter, *J. Phys. Chem. C*, 2011, **115**, 2656–2664.

5 S. H. Sun, C. B. Murray, D. Weller, L. Folks and A. Moser, *Science*, 2000, **287**, 1989–1992.

This journal is © the Owner Societies 2015

*Phys. Chem. Chem. Phys.*, 2015, **17**, 1070–1076 | 1075

6  N. Wu, L. Fu, M. Su, M. Aslam, K. C. Wong and V. P. Dravid, *Nano Lett.*, 2004, **4**, 383–386.

7  D. Amans, C. Malaterre, M. Diouf, C. Mancini, F. Chaput, G. Ledoux, G. Breton, Y. Guillin, C. Dujardin, K. Masenelli-Varlot and P. Perriat, *J. Phys. Chem. C*, 2011, **115**, 5131–5139.

8  S. E. Skrabalak, B. J. Wiley, M. Kim, E. V. Formo and Y. Xia, *Nano Lett.*, 2008, **8**, 2077–2081.

9  S. I. Cha, C. B. Mo, K. T. Kim, Y. J. Jeong and S. H. Hong, *J. Mater. Res.*, 2006, **21**, 2371–2378.

10  Y. Xiong, H. Cai, B. J. Wiley, J. Wang, M. J. Kim and Y. Xia, *J. Am. Chem. Soc.*, 2007, **129**, 3665–3675.

11  G. Sankar, P. A. Wright, S. Natarajan, J. M. Thomas, G. N. Greaves, A. J. Dent, B. R. Dobson, C. A. Ramsdale and R. H. Jones, *J. Phys. Chem.*, 1993, **97**, 9550–9554.

12  M. Harada and Y. Kamigaito, *Langmuir*, 2011, **28**, 2415–2428.

13  M. Harada, N. Tamura and M. Takenaka, *J. Phys. Chem. C*, 2011, **115**, 14081–14092.

14  M. Harada and Y. Inada, *Langmuir*, 2009, **25**, 6049–6061.

15  K. K. Bando, T. Wada, T. Miyamoto, K. Miyazaki, S. Takakusagi, Y. Koike, Y. Inada, M. Nomura, A. Yamaguchi, T. Gott, S. T. Oyama and K. Asakura, *J. Catal.*, 2012, **286**, 165–171.

16  A. Caballero, A. R. Gonzalezelipe, A. Fernandez, J. M. Herrmann, H. Dexpert and F. Villain, *J. Photochem. Photobiol., A*, 1994, **78**, 169–172.

17  F. Fievet, J. P. Lagier, B. Blin, B. Beaudoin and M. Figlarz, *Solid State Ionics*, 1989, **32–33**, 198–205.

18  F. Fiévet and R. Brayner, in *Nanomaterials: A Danger or a Promise?* ed. R. Brayner, F. Fiévet and T. Coradin, Springer, London, 2013, ch. 1, pp. 1–25.

19  G. P. P. Pun and Y. Mishin, *Phys. Rev. B: Condens. Matter Mater. Phys.*, 2012, **86**, 134116.

20  P. Tolédano, G. Krexner, M. Prem, H. P. Weber and V. P. Dmitriev, *Phys. Rev. B: Condens. Matter Mater. Phys.*, 2001, **64**, 144104.

21  M. M. J. Treacy, J. M. Newsam and M. W. Deem, *Proc. R. Soc. London, Ser. A*, 1991, **433**, 499–520.

22  P. W. Stephens, *J. Appl. Crystallogr.*, 1999, **32**, 281–289.

23  J. Garcia-Otero, M. Porto and J. Rivas, *J. Appl. Phys.*, 2000, **87**, 7376–7381.

24  E. P. Wohlfarth, *J. Appl. Phys.*, 1958, **29**, 595.

25  R. W. Gao, W. Chen, J. C. Zhang, W. C. Fong, W. Li and X. M. Li, *J. Mater. Sci. Technol.*, 2001, **17**, S93–S96.

26  C. R. Pike, A. P. Roberts and K. L. Verosub, *J. Appl. Phys.*, 1999, **85**, 6660–6667.

27  A. P. Roberts, C. R. Pike and K. L. Verosub, *J. Geophys. Res.: Solid Earth*, 2000, **105**, 28461–28475.

28  J. E. Davies, J. Wu, C. Leighton and K. Liu, *Phys. Rev. B: Condens. Matter Mater. Phys.*, 2005, **72**, 134419.

29  V. K. LaMer and R. H. Dinegar, *J. Am. Chem. Soc.*, 1950, **72**, 4847–4854.

30  M. Avrami, *J. Chem. Phys.*, 1939, **7**, 1103–1112.

31  M. Avrami, *J. Chem. Phys.*, 1941, **9**, 177–184.

32  M. A. Watzky and R. G. Finke, *J. Am. Chem. Soc.*, 1997, **119**, 10382–10400.

33  D. Kodama, K. Shinoda, K. Sato, Y. Sato, B. Jeyadevan and K. Tohji, *J. Magn. Magn. Mater.*, 2007, **310**, 2396–2398.

34  J. Cheng, P. Hu, P. Ellis, S. French, G. Kelly and C. M. Lok, *J. Phys. Chem. C*, 2009, **114**, 1085–1093.

35  S. Stolbov, S. Hong, A. Kara and T. S. Rahman, *Phys. Rev. B: Condens. Matter Mater. Phys.*, 2005, **72**, 155423.

36  N. E. Tsakoumis, M. Ronning, O. Borg, E. Rytter and A. Holmen, *Catal. Today*, 2010, **154**, 162–182.

37  J. Lahiri, T. Miller, L. Adamska, I. I. Oleynik and M. Batzill, *Nano Lett.*, 2010, **11**, 518–522.

38  J. Baumgartner, A. Dey, P. H. Bomans, C. Le Coadou, P. Fratzl, N. A. Sommerdijk and D. Faivre, *Nat. Mater.*, 2013, **12**, 310–314.

39  R. Lacmann, *Chem. Ing. Tech.*, 1998, **70**, 1468.